LITHOS 460–461 (2023) 107375

Contents lists available at ScienceDirect

LITHOS

journal homepage: www.elsevier.com/locate/lithos

Pseudotachylytes in felsic lower-crustal rocks of the Calabrian Serre massif: A record of deep- or shallow-crustal earthquakes?

Simone Papa [a], Giorgio Pennacchioni [a,*], Alfredo Camacho [b], Kyle P. Larson [c]

[a] Department of Geosciences, University of Padua, Via G. Gradenigo 6, 35131 Padua, Italy
[b] Department of Earth Sciences, University of Manitoba, Winnipeg, MB, Canada
[c] Department of Earth, Environmental and Geographic Sciences, University of British Columbia, Okanagan, Kelowna, BC, Canada

ARTICLE INFO

Keywords:
Pseudotachylyte
Lower-crustal granulites
Microlites
In situ Rb-Sr dating
Modelling of melt quenching and cordierite growth

ABSTRACT

Pseudotachylytes (quenched frictional melts produced on a fault by seismic slip) in dry rocks exhumed from the mid-lower crust are potential indicators of earthquakes that either nucleated at, or propagated to, depths below the main shallow brittle-ductile transition zone. Establishing whether these pseudotachylytes effectively record deep-crustal earthquakes, or shallow-level earthquakes overprinting the mid-lower-crustal rocks during the exhumation path, may represent a major challenge. This challenge is mainly related to the fact that the mineral assemblage of a pseudotachylyte develops out of equilibrium during the coseismic thermal transient leading to melting and melt quenching. Here we investigate pseudotachylytes within peraluminous, sillimanite-garnet-rich, migmatitic paragneiss of the Serre Massif in Calabria (Southern Italy). These exhumed lower-crustal rocks experienced granulite-facies metamorphism (~700–800 °C; ~600–800 MPa), partial melting and dehydration during the late Variscan Orogeny (ca. 320–280 Ma). The crosscutting pseudotachylytes contain hercynite and sillimanite microlites, globular-shaped poikilitic cordierite and plagioclase, and rare cauliflower- to subhedral-shaped garnet. The pseudotachylytes are pristine, not affected by ductile deformation, recrystallisation or extensive alteration by fluid after their formation. A Rb-Sr isochron age of 51.4 ± 5.1 Ma is obtained for the pervasively kinked biotite in the host rock immediately adjacent to the pseudotachylyte and associated with earthquake damage, while an age of 105.3 ± 4.1 Ma is obtained for the undeformed host-rock biotite. This indicates that the granulites were cooler than the closing Rb-Sr temperature of biotite (ca. 300–400 °C) in the Cretaceous and that the studied pseudotachylytes formed by shallow seismic faulting. Therefore, sillimanite, hercynite, garnet, plagioclase, and cordierite all formed during quenching of the frictional melt well above the ambient temperature. Modelling of cordierite growth during melt quenching indicates that cordierite should have started to crystallise at $T > 900$ °C to achieve the grain size (up to 10 μm in diameter) observed in the pseudotachylyte. Modelling and microstructural observations allow the crystallisation sequence of microlites during melt cooling to be established. These microlites include cauliflower garnet which, in this case, did not develop in a deep-seated faulting context as commonly reported.

1. Introduction

Pseudotachylytes (quenched frictional melts produced on a fault in silicate rocks by seismic slip) are fault rocks typically formed near the base of the brittle upper crust. However, locally conspicuous volumes of pseudotachylytes have also been reported from exhumed dry lower-crustal continental rocks and interpreted in many cases as the geological record of deep-crustal earthquakes (Austrheim et al., 1996; Austrheim and Boundy, 1994; Campbell et al., 2020; Hawemann et al., 2018; Menegon et al., 2017). The geometry and microstructures of pseudotachylyte-bearing faults may preserve the record of the complex sequence of deformation and thermal events that occur during the short-lived (seconds to minutes) event of an earthquake, including the stages of earthquake rupture propagation, and seismic fault slip with production of frictional melts and melt quenching (Brückner and Trepmann, 2021; Campbell and Menegon, 2022; Dunkel et al., 2020; Mancktelow et al., 2022; Petley-Ragan et al., 2019). The study of pseudotachylytes is therefore a fundamental tool for investigating the mechanics of a seismic source in either shallow or deep environments (Beeler et al., 2016; Di Toro et al., 2005a, 2005b; Johnson et al., 2021; Lazari et al., 2023;

* Corresponding author.
E-mail address: giorgio.pennacchioni@unipd.it (G. Pennacchioni).

https://doi.org/10.1016/j.lithos.2023.107375
Received 12 April 2023; Received in revised form 22 September 2023; Accepted 2 October 2023
Available online 4 October 2023

Pittarello et al., 2008; Sibson, 1975). Many of the estimates of mechanical parameters of an earthquake, determined from pseudotachylyte-bearing faults, are based on quantitative analysis of microstructures within the pseudotachylyte and in the immediately adjacent damaged host rock. Unfortunately, these pristine, fine-grained, coseismic microstructures are easily erased due to alteration and deformation following the pseudotachylyte formation and during the exhumation path to the Earth's surface (Fondriest et al., 2020; Kirkpatrick and Rowe, 2013). Obliteration of coseismic microstructures is especially favoured for deep-seated pseudotachylytes (i.e. formed beneath, and at higher temperature than, the typical depth of brittle-ductile transition of rocks) because of the longer exhumation path and of contingent overprint by ductile flow at the high-temperature conditions of formation. However, deep-seated pseudotachylytes are commonly hosted in dry rocks that are strong and yield by brittle (seismic) failure even at high temperature, at which equivalent water-bearing rocks would flow ductilely (Austrheim, 1987; Jackson et al., 2004). Therefore, deep-seated pseudotachylytes hosted in dry rocks can survive metamorphic re-equilibration and be preserved metastably (Dunkel et al., 2021; Pennacchioni et al., 2020).

If dry conditions promote seismicity at depth and the preservation of pristine pseudotachylytes, in absence of a concurring ductile deformation and metamorphic re-equilibration it is difficult to establish whether pseudotachylytes hosted in dry exhumed lower-crustal rocks formed by deep or shallow earthquakes. The mineral assemblage of a pseudotachylyte forms out of equilibrium at undercooling conditions, during the high temperature spike of frictional melting and the following quenching (Spray, 2010). Therefore, the mineral assemblage may well not be diagnostic of the ambient conditions of faulting.

Here we report a new locality, near Amaroni village in the Serre massif of Calabria (Southern Italy), where lower-crustal migmatitic paragneiss are crosscut by well preserved pseudotachylytes. The pseudotachylytes contain hercynite and sillimanite microlites, globular-shaped poikilitic cordierite and plagioclase, and cauliflower- to subhedral-shaped garnet.

We integrate different types of analysis to infer the environment of seismic faulting: (i) high-resolution microstructural analysis by scanning electron microscopy; (ii) geochronological (Rb-Sr) dating; and (iii) modelling of the thermal transient associated with frictional slip and of the growth of cordierite crystals. Our study indicates that the pseudotachylytes are Alpine in age and overprinted, at upper crustal levels, lower-crustal granulites that had already been uplifted to 10–15 km depth at the end of the Variscan orogeny (Schenk, 1980, 1984) and cooled down to <300–400 °C. Our findings highlight the intrinsic uncertainty in determining the ambient conditions of pseudotachylyte formation. The mineral composition of pristine pseudotachylyte (e.g. the occurrence of garnet microlites) must be used with caution in the identification of a lower-crustal origin of seismic faulting.

2. Geological setting of the Serre Massif

The Serre Massif (Calabria, southern Italy) exposes a cross-section of Variscan, upper to lower continental crust (Fig. 1a-c; Schenk, 1980). Schenk (1980) subdivided the granulitic lower-crustal section into a *granulite-pyriclasite unit* underneath an Al-rich *metapelite unit* (Fig. 1c). Altenberger et al. (2013) studied pseudotachylytes from both units and concluded that they originated at deep crustal conditions. The *metapelite unit* is mostly made of migmatitic paragneisses composed of biotite, sillimanite, plagioclase, quartz, garnet, cordierite, K-feldspar, and ilmenite/rutile (Schenk, 1984). Peak metamorphic conditions of 700–800 °C at 600–900 MPa (Fig. 1d; Schenk, 1989; Acquafredda et al., 2006, 2008; Festa et al., 2012) were coeval to partial melting with a loss of melt from migmatitic metapelite estimated to about 40 wt% by Schenk (1990) and 27–66 vol% by Fornelli et al. (2002). Published P-T-t paths (Fig. 1d) show that, after the peak granulite-facies metamorphism, during the late stages of the Variscan orogeny, the Serre lower crustal units underwent fast, nearly isothermal decompression (280–320 Ma: Schenk, 1989; Acquafredda et al., 2006). Decompression was interpreted to have occurred either in an extensional (Acquafredda et al., 2006; Caggianelli et al., 2000; Del Moro et al., 2000) or in a compressional regime (Schenk, 1980, 1984) and was followed by slow isobaric cooling (Schenk, 1980, 1984, 1989). Del Moro et al. (2000) obtained Rb-Sr biotite ages of ca. 110 Ma for the Serre rocks that can be interpreted as indicative of either continuous isobaric cooling (Schenk, 1984, 1989) or discrete tectonic events in the Mesozoic (Del Moro et al., 1986, 2000).

Toward the NW, the Serre lower-crustal rocks are juxtaposed onto Variscan amphibolite-facies orthogneisses of the Castagna Unit (Fig. 1c) along a mylonitic thrust (*Curinga-Girifalco Line*: *CGL*). Schenk (1980) obtained a Rb-Sr age of biotite of 43 ± 1 Ma on a mylonitic gneiss of the Castagna Unit, indicating *CGL* activity of Alpine age (Brandt and Schenk, 2020; Festa et al., 2020). The mylonites, especially those derived from the Serre dry lower-crustal rocks, contain interspersed, abundant, syn- to post-kinematic pseudotachylytes (Altenberger et al., 2013). Langone et al. (2006) and Brandt and Schenk (2020) estimated the deformation conditions in the footwall of the *CGL* at 500–600 °C and 700–900 MPa (Fig. 1d). Pressure and temperature conditions in the Serre rocks of the *CGL* hanging wall are difficult to estimate due to scarce re-equilibration under dry conditions. Garnet growth in syn-mylonitic pseudotachylytes was interpreted by Altenberger et al. (2013) as evidence for high pressure during deformation, consistent with the thermo-barometric estimates in the footwall. Instead, no cordierite grew during Alpine mylonitisation; the cordierite porphyroclasts occurring in the *CGL* mylonites are interpreted as relicts, preserved under dry conditions (Spiegel, 2003). Brandt and Schenk (2020) ascribed the Alpine overprint in the footwall of the *CGL* to shear heating and tectonic loading during thrusting of the Serre hanging wall that, instead, had remained at <300–400 °C (approximate closure temperature of biotite: Armstrong et al., 1966; Verschure et al., 1980) since 110 Ma, as biotite ages were not rejuvenated during Alpine thrusting (Schenk, 1980).

3. Methods

Thin sections of pseudotachylytes were investigated using a Tescan Solaris Field-Emission Scanning Electron Microscope (FE-SEM). Images were acquired with a mid-angle backscattered detector at working conditions of: 5 KeV acceleration voltage, 300 pA beam current, and 4 mm working distance. Chemical point analyses and maps were obtained with the Ultim max 65 Oxford Instrument silicon drift EDS (Energy Dispersive Spectroscopy), at working conditions of: 15 KeV acceleration voltage, 3 nA beam current, and 5 mm working distance. Since the pseudotachylyte minerals are intergrown at a finer scale than the spot size of high-resolution ED-WD (Energy Dispersive-Wavelength Dispersive) spectrometry (~ 0.7 μm), the chemical compositions of matrix phases show a certain degree of contamination. Electron Backscattered Diffraction (EBSD) maps were acquired with an Oxford Instruments Symmetry S2 detector, equipped with a CMOS sensor, with working conditions of: 20 KeV acceleration voltage, 10 nA beam current, and 200 nm step size.

X-Ray Powder Diffraction (XRPD) measurements were performed using a Philips X'Pert Pro MPD diffractometer, equipped with a long-fine-focus cobalt anode tube working at: 40 kV, 40 mA, and a 240 mm goniometer radius that operates in the θ/θ geometry. Measurements were carried out, between 3° and 85° 2θ angle, using: 0.017° step size and 100 s counting time per virtual step on a circular, 27 mm diameter, spinning sample (1 revolution per second). Samples were prepared using the back-loading procedure in order to reduce preferred orientations of crystallites. Mineralogical species were identified using PANalytical High Score Plus v.4.8.0 (Malvern Panalytical Ltd., Malvern, UK). Semi-quantitative analysis was performed using the Normalized Reference Intensity Ratio (normalized RIR) method as implemented in High Score Plus, considering preferred orientations of certain crystallographic directions that led to complex distribution of intensities. Calculated

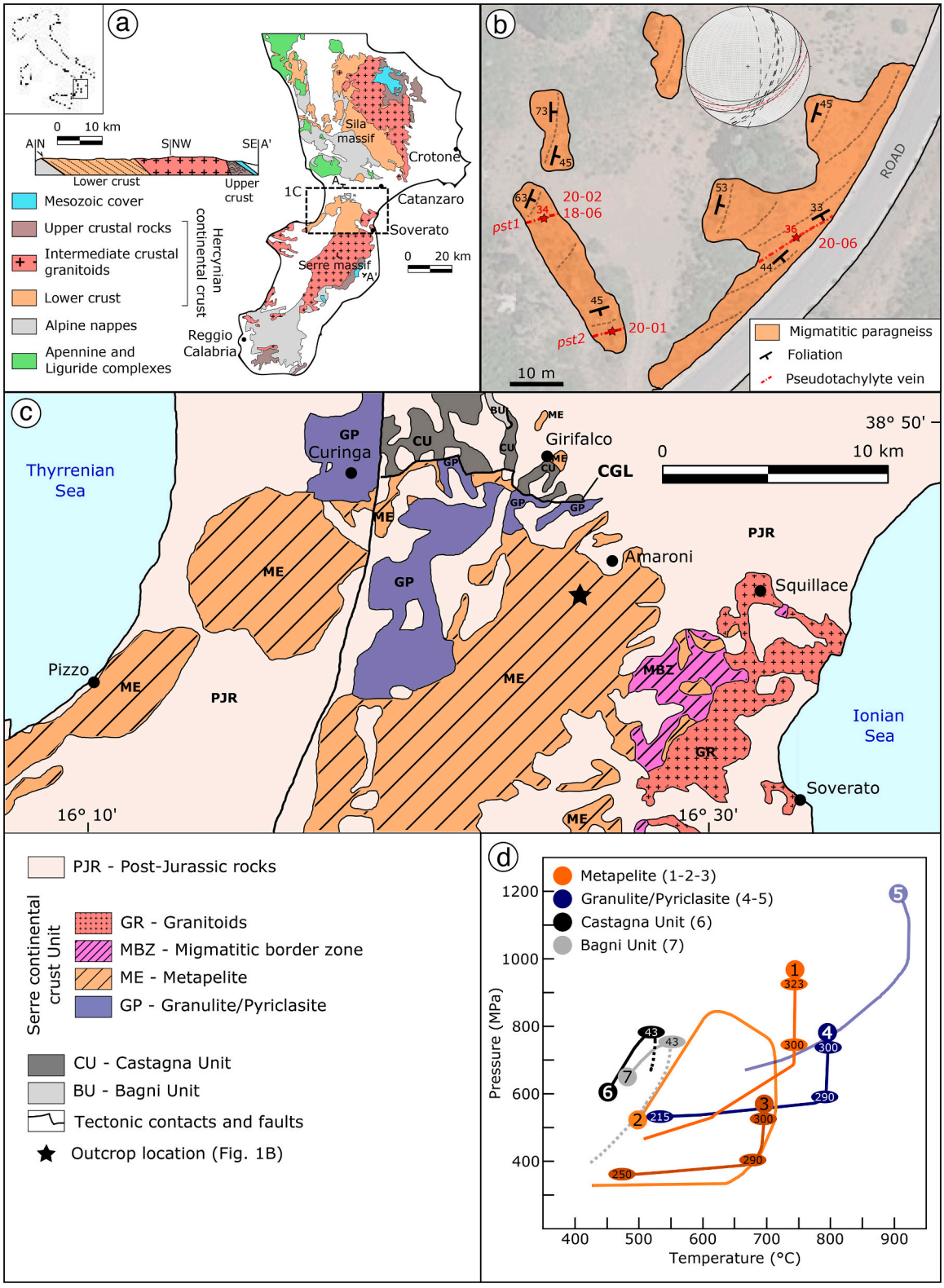

Fig. 1. (a) Simplified geological map of Calabria (modified after Brandt and Schenk (2020) and references therein) and geological cross-section showing the structure of the crustal units exposed in the Serre Massif (after Schenk (1984) and references therein). (b) Sketch of the studied outcrop. Location of the outcrop (N 38° 46′ 43″; E 16° 25′ 41″) is shown by the star in (c). Gray dashed lines indicate the strike of the host-rock granulite foliation; red dashed-dotted lines indicate the strike of the two pseudotachylyte-bearing faults; red stars indicate the location of the studied samples. The stereoplot reports the orientations of pseudotachylytes (red dashed-dotted curves), host-rock foliations (black dashed curves), and the host-rock foliations close to the pseudotachylytes (black solid curves). (c) Simplified geological map of the northern portion of the Serre Massif (modified from Caggianelli et al. (2013) and references therein). CGL: Curinga-Girifalco Line. (d) P-T-t paths for the Serre metapelite unit (in orange) and granulite-pyriclasite unit (in blue), Castagna unit (black) and Bagni unit (gray). Numbers in the oval frame indicate ages in Ma. Data from: (1) Festa et al. (2012); (2) Acquafredda et al. (2006); (3–4) Schenk (1989); (5) Acquafredda et al. (2008); (6–7) Brandt and Schenk (2020). (For interpretation of the references to colour in this figure legend, the reader is referred to the web version of this article.)

weight fractions are based on the scale factor, which is determined by a least-squares fit through all matching reference pattern lines and avoiding any pattern shift that strongly influences the scale factors and the semi-quantitative results. All the instruments are at the Department of Geosciences of the University of Padova.

Rb-Sr in-situ LA-ICP-MS analyses were performed via triple quadrupole inductively coupled plasma mass spectrometry at the Fipke Laboratory for Trace Element Research (FiLTER) at the University of British Columbia Okanagan using the analytical procedure developed by Zack and Hogmalm (2016), Hogmalm et al. (2017) and Redaa et al. (2021) as described in Larson et al. (2023). Repeat analyses of the pressed nano-powder MICA Fe as a secondary reference material during analytical runs define an isochron of 305 ± 3 Ma, which overlaps the expected age of 305 ± 2 (Rösel and Zack, 2022). Possible matrix fractionation between mica crystals and pressed nano-powders is unresolvable at the precision level of the analyses (e.g. Larson et al., 2023).

4. Pseudotachylyte description

4.1. Field observations

Pseudotachylytes were sampled at a location about 4 km south of the *CGL*, close to the village of Amaroni (Fig. 1b; N 38° 46′ 43″; E 16° 25′ 41″). Outcrop conditions in the area are generally poor, but this location provides isolated exposures of non-weathered rocks due to recent clearing and road works. The pseudotachylytes are within foliated, lower-crustal migmatitic paragneisses made up of quartz, garnet, biotite, sillimanite, plagioclase, K-feldspar, and local cordierite (Fig. 2a). Feldspar and quartz form leucosome layers that anastomose around the volumetrically predominant garnet-biotite-sillimanite melanosomes. Garnet occurs as abundant, coarse (grain size of as much as 10 cm) poikiloblasts. Similar metapelites with coarse garnet porphyroblasts were mapped in an horizon, between the villages of Monterosso and Capistrano, that can be followed over a distance of >10 km (Schenk, 1984). The migmatitic foliation dips toward ESE (Fig. 1b), consistently with the orientation of the dominant granulitic foliation in the Serre unit (Kruhl and Huntemann, 1991).

Pseudotachylyte fault veins dip moderately (35–45°) toward SSE and sharply cross-cut the migmatitic foliation (Fig. 1b). The foliation is rotated in the vicinity of pseudotachylyte veins (Fig. 1b) and the geometry indicates a normal component of shear. Two distinct, subparallel pseudotachylyte-bearing faults (hereafter referred to as pst_1 and pst_2), spaced a few tens of meters apart, were sampled (Fig. 1b).

The outcrop of pst_1 displays a surface nearly coincident with the fault vein, with irregular patches of gray-coloured (black where freshly broken) pseudotachylyte. The irregular 2D geometry results from the presence of a network of injection veins (Fig. 2c). Pst_1 contains clusters of mm-sized quartz and sillimanite clasts of equant shape and locally shows convolute flow (magmatic) structures. Pst_2 is an individual fault vein, without prominent injection veins, with a slightly sinuous shape

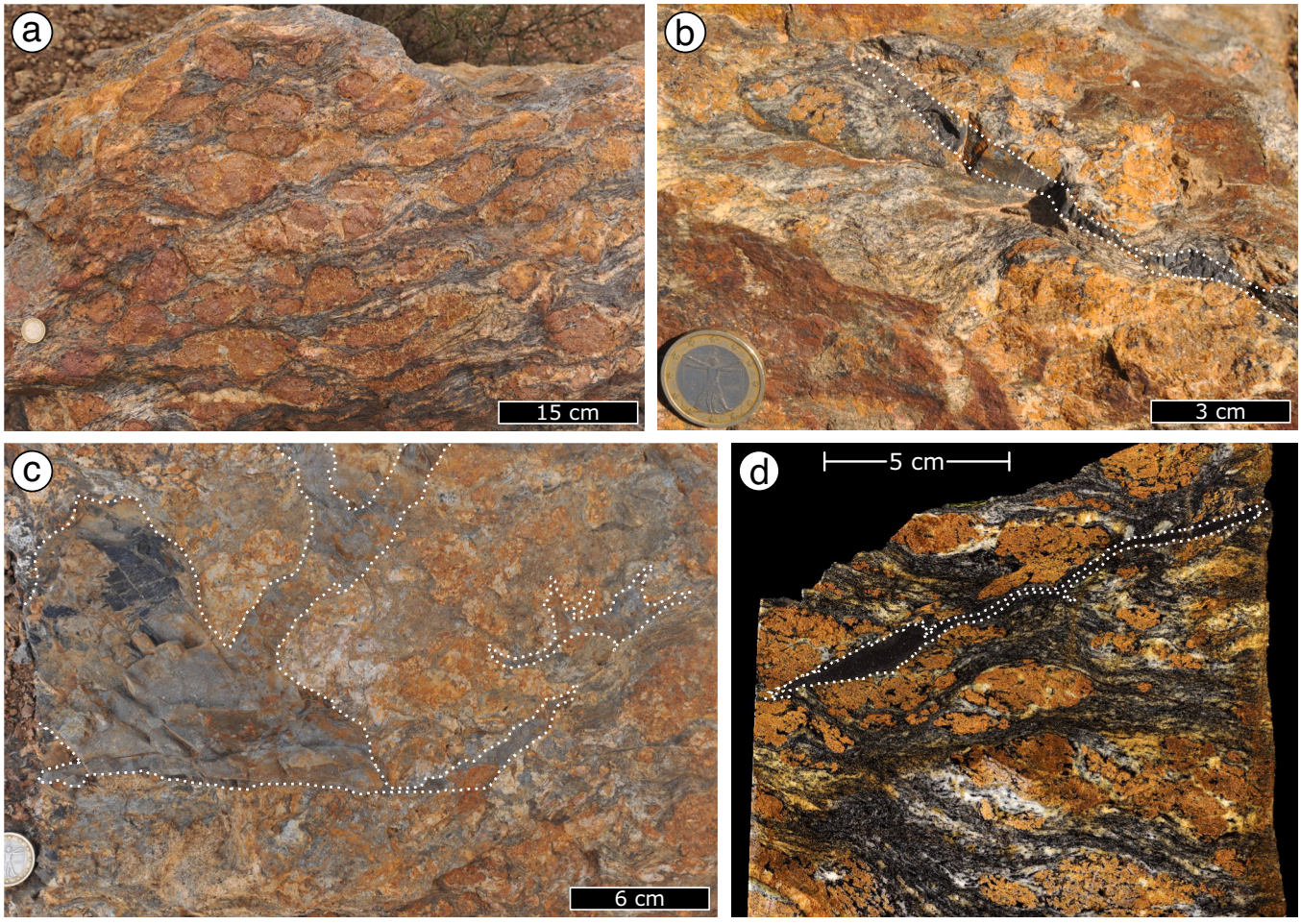

Fig. 2. Field and sample images of the granulite host-rock and pseudotachylytes. (a) Migmatitic paragneiss showing large reddish porphyroblasts of garnets, wrapped around by blueish (sillimanite-biotite-rich melanosomes) and white (quartz-feldspar-rich leucosomes) layers marking the migmatitic foliation. (b) Pst_2, outlined by the white dotted line (sample 20–01). (c) Pst_1, outlined by the white dotted line, with irregular, branching geometry. (d) Pst_2 (sample 20–01) crosscutting discordantly the granulite foliation. Polished slab cut orthogonal to the pseudotachylyte vein. (For interpretation of the references to colour in this figure legend, the reader is referred to the web version of this article.)

and variable thickness (max. 5 mm) over the short outcrop exposure of 30 cm (Fig. 2b, d) in the western outcrop. Both pseudotachylytes are single-jerk veins (sensu Sibson, 1975), i.e. they do not show evidence of multiple events of frictional melting.

4.2. Pseudotachylyte microstructure and petrography

4.2.1. Pst_1: Samples 18–06 and 20–02

Pseudotachylyte microlites and flow structures (defined by a compositional layering) are well preserved without evidence of solid-state, post-seismic ductile deformation (Fig. 3a-d). Semi-quantitative XRPD analysis of the bulk (i.e. including clasts) pseudotachylyte of sample 20–02 detected quartz (39%), hercynite (19%), plagioclase (19%), cordierite (11%), biotite (6%), sillimanite (6%), and ilmenite (1%). Clasts mainly consist of quartz and sillimanite. Garnet clasts and microlites were not observed at any scale, although the host rock is mostly made of large garnet porphyroblasts. In contact with the pseudotachylyte, the host-rock garnet shows an intense fragmentation as commonly observed in other pseudotachylyte-bearing rocks (Austrheim et al., 2017; Papa et al., 2018).

Primary flow banding is defined by the alternation of two distinct compositional domains (referred to as α and β; Fig. 3a). Domain α, making up most of the vein, consists of an optically dark and isotropic matrix including densely-packed hercynite microlites. Hercynite occurs as either relatively large (max 5 μm grain size; Fig. 3b-d) granular microlites or smaller dendritic, cross-shaped to acicular ones (Fig. 3c). In areas where hercynite microlites are more sparsely distributed, larger granular shapes dominate in association with feathery microlites (5–10 μm in size) of a Fe-Al-Mg silicate (Fig. 3d). The feathery microlites are similar in morphology and chemical composition to orthoamphibole (ferrogedrite) microlites reported in other metapelite-hosted pseudotachylytes (Ray, 2004). Orthoamphibole was not detected by XRPD probably due to its very low abundance. Microlites are surrounded by aggregates of micrometre-sized biotite, plagioclase, quartz and ilmenite.

Domain β is characterised by microlites and globular poikilitic grains set in a seemingly homogeneous, "glassy" matrix, brownish and transparent under polarised light (Fig. 3b). High-magnification BSE images and high-resolution chemical analyses show that the matrix contains very small (100–200 nm in diameter), silica-rich (likely quartz) grains. Raman spectra of the matrix show peaks characteristic of quartz, biotite and, locally, muscovite. Hercynite microlites are larger (max 10–20 μm), commonly granular or stellate in shape, and more sparsely distributed than in domain α (Fig. 3a, c). Domain β is characterised by acicular aluminosilicate microlites, locally up to 100 μm in length (Figs. 3c, 4), that commonly nucleated over sillimanite clasts and are locally overgrown by micrometre-sized dendritic hercynite microlites (Fig. 4). EBSD maps show that the acicular microlites are in crystallographic continuity with their seed sillimanite clasts and the elongation of these epitaxial microlites is parallel to the [001] axis (Fig. 4e, f). The microlites could not be identified by Raman spectroscopy because of their very fine grain size; by EBSD they were equally well indexed as either sillimanite or mullite (Fig. 4d). Chemically, these microlites are approximately stoichiometric Al_2SiO_5, while ideal mullite has a stoichiometric composition of $3Al_2O_3{\cdot}2SiO_2$. However, Moecher and Brearley (2004) have shown by TEM analysis that mullite microlites in pseudotachylytes can have a chemical composition poorer in Al than ideal mullite and very similar to the microlites analysed here. However, considering the identical chemical composition and crystallographic continuity with the seed sillimanite clasts, it seems reasonable to conclude that microlites are most likely sillimanite.

In domain β, microlites are commonly surrounded by locally intergrown Ca-rich plagioclase (andesine: An_{38}) and cordierite ($X_{Fe} = 0.26$) grains, 2–10 μm in diameter, and with spherical to slightly ellipsoidal shape (Fig. 3c). These globular grains are rich in inclusions of hercynite and other matrix minerals, especially in their core, and occur either isolated in the matrix or, more commonly, in clusters. EBSD maps show that these grains, also in clusters, consist of single crystals of either cordierite or plagioclase with distinct crystallographic orientation across the pseudotachylyte. When cordierite and plagioclase grains are in direct contact, a systematic order of crystallisation cannot be established (unlabelled white arrows in Fig. 3c).

4.2.2. Pst_2: Sample 20–01 and 20–06

The pseudotachylyte (sample 20–01) is homogeneous and mostly made of granular hercynite microlites (<2 μm in size) and globular cordierite grains set in a biotite matrix (Fig. 3e-f). Cordierite, up to 20 μm in diameter, includes abundant hercynite microlites (Fig. 3e-f). The matrix also contains submicrometric grains of sulphides and iron oxides. The abundant host rock clasts mostly consist of quartz and sillimanite, and minor K-feldspar. No sillimanite microlites have been observed. Semi-quantitative bulk XRPD analysis has detected sillimanite (32%), quartz (27%), biotite (17%), hercynite (12%), cordierite (5%) and minor amounts of ilmenite, almandine, K-feldspar and kaolinite.

In sample 20–01, a thin (max. 200 μm thick) injection vein cuts across a large host-rock garnet. At the contact with the pseudotachylyte, the host-rock garnet is fragmented down to the submicrometric scale and the vein contains garnet microlites with the typical 'cauliflower' dendritic morphology described in several deep-crustal pseudotachylytes (Figs. 5, 6) (Altenberger et al., 2013; Dunkel et al., 2020; Hawemann et al., 2018; Lund and Austrheim, 2003; Mancktelow et al., 2022; Pittarello et al., 2012). The size of the garnet cauliflowers increases from the margin toward the centre of the vein to sizes of as much as 50 μm (Fig. 5a). Locally, garnet microlites show plane crystal facets (white arrows in Fig. 6b, c). Microlitic garnets, irrespective of their shape and size, contain abundant tiny inclusions, contrary to the host-rock garnet. At least three types of inclusions can be distinguished (Fig. 6d): (i) bright (in SEM-BSE images) and euhedral, resembling hercynite microlites (white arrows in Fig. 6d); (ii) brighter spherical to vermicular, resembling sulfides (commonly reported in pseudotachylytes: e.g. Magloughlin, 2005; red arrows in Fig. 6d); (iii) dark and locally faceted (black arrows in Fig. 6d). In some cases, garnet microlites show an inclusion-free host-rock clast at their core (Fig. 6a, c).

EBSD maps show that the "branches" of the larger 'cauliflower' garnets in the vein centre inherited the crystallographic orientation of the garnet clast seed, with only minor continuous variation (Fig. 5g). In other instances, especially for smaller garnets closer to the pseudotachylyte border, EBSD maps reveal that the apparent cauliflower is a cluster of single crystals with different crystallographic orientations (Fig. 5h), probably reflecting the higher abundance of preserved host-rock garnet clasts at the quenched vein margins.

Garnet microlites commonly show irregular, resorbed grain boundaries, with an evident black outline, surrounded by a 'corona', similar in colour in SEM-BSE images to the garnet, and rich in the same kind of inclusions (Fig. 6). These coronae locally are bounded by regular crystal facets (Fig. 6a-c), indicating that they result from the static replacement of the original garnet microlite.

EDS analyses and maps (Fig. 5c-f; supplementary material) show that the host-rock garnet is predominantly almandine ($Alm_{65}Pyr_{31}$) while the cataclastic garnet close to pseudotachylyte boundary is slightly enriched in Fe ($Alm_{69}Pyr_{26}$). In comparison with the host-rock garnet, garnet microlites ($Alm_{82}Pyr_{13}$) are enriched in Fe (Fig. 5d), depleted in Mg (Fig. 5c) and slightly enriched in Mn (from 1 mol% spessartine in the host rock to locally 3 mol% in the microlites; see supplementary material). In addition, the microlites are compositionally uniform (15 point analyses) and minor compositional variations are likely due contamination from inclusions. The alteration product of garnet is a Mg-free, hydrous aluminium silicate of Fe (Fig. 5c-f), probably Fe-rich chlorite (chamosite). Apart from the localised occurrence of garnet in sample 20–01, all the other studied pseudotachylytes are free of garnet clasts and microlites.

Sample 20–06 was selected for Rb-Sr dating of the host rock biotite. The pristine, coarse, granulite facies biotite occurs, distant from the

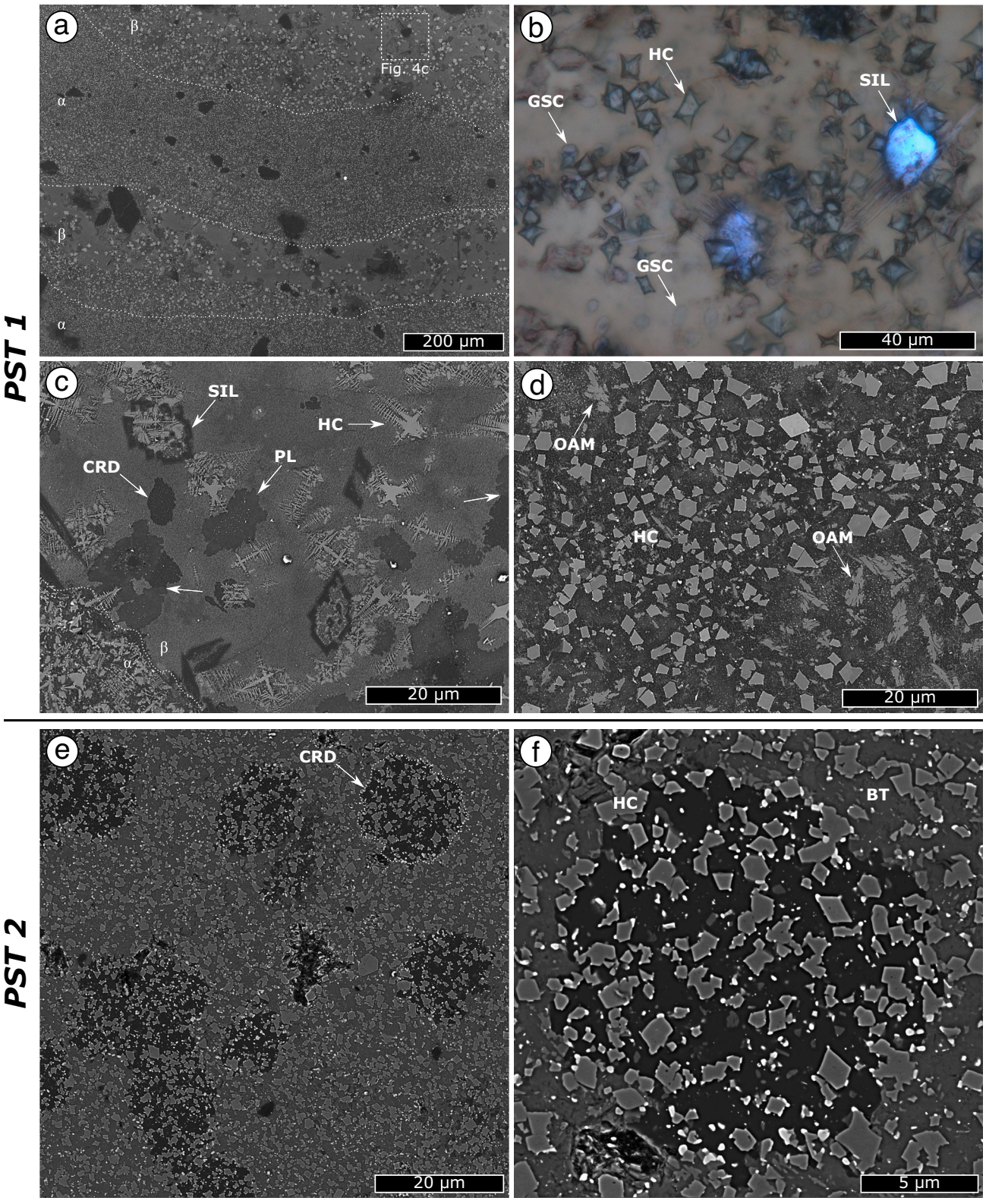

Fig. 3. Microstructures of pst_1 and pst_2. (a) Alternation of domains α and β in pst_1, defining the flow banding. The boundaries between the two domains, highlighted by white dotted lines, are characterised by a change in grain size of hercynite microlites. SEM-BSE image. (b) Domain β of pst_1 showing abundant microlites of hercynite (HC) and acicular sillimanite overgrowing sillimanite clasts (SIL), and globular-shaped crystals (GSC) within a "glassy" homogeneous matrix. Optical microscope; plane-polarised light. (c) Similar type of microstructure as in (b) in SEM-BSE image. Unlabelled white arrows indicate contacts between irregular-globular poikilitic grains of cordierite and (lighter gray) plagioclase. In the lower left corner of the image, the microstructure transitions to domain α with densely-packed, granular hercynite microlites. (d) Domain α of pst_1 showing abundant granular hercynite microlites and feathery orthoamphibole microlites. SEM-BSE image. (e) Pst_2 showing hercynite microlites, cordierite globular poikiloblasts (one is outlined by a dotted white line) and biotite-rich matrix. SEM-BSE image. (f) Detail of the cordierite globular poikiloblasts, outlined (dotted line) in (e), with abundant inclusions of hercynite microlites. Abbreviations: HC = hercynite; SIL = sillimanite; GSC = globular-shaped crystal; CRD = cordierite; PL = plagioclase; OAM = orthoamphibole; BT = biotite.

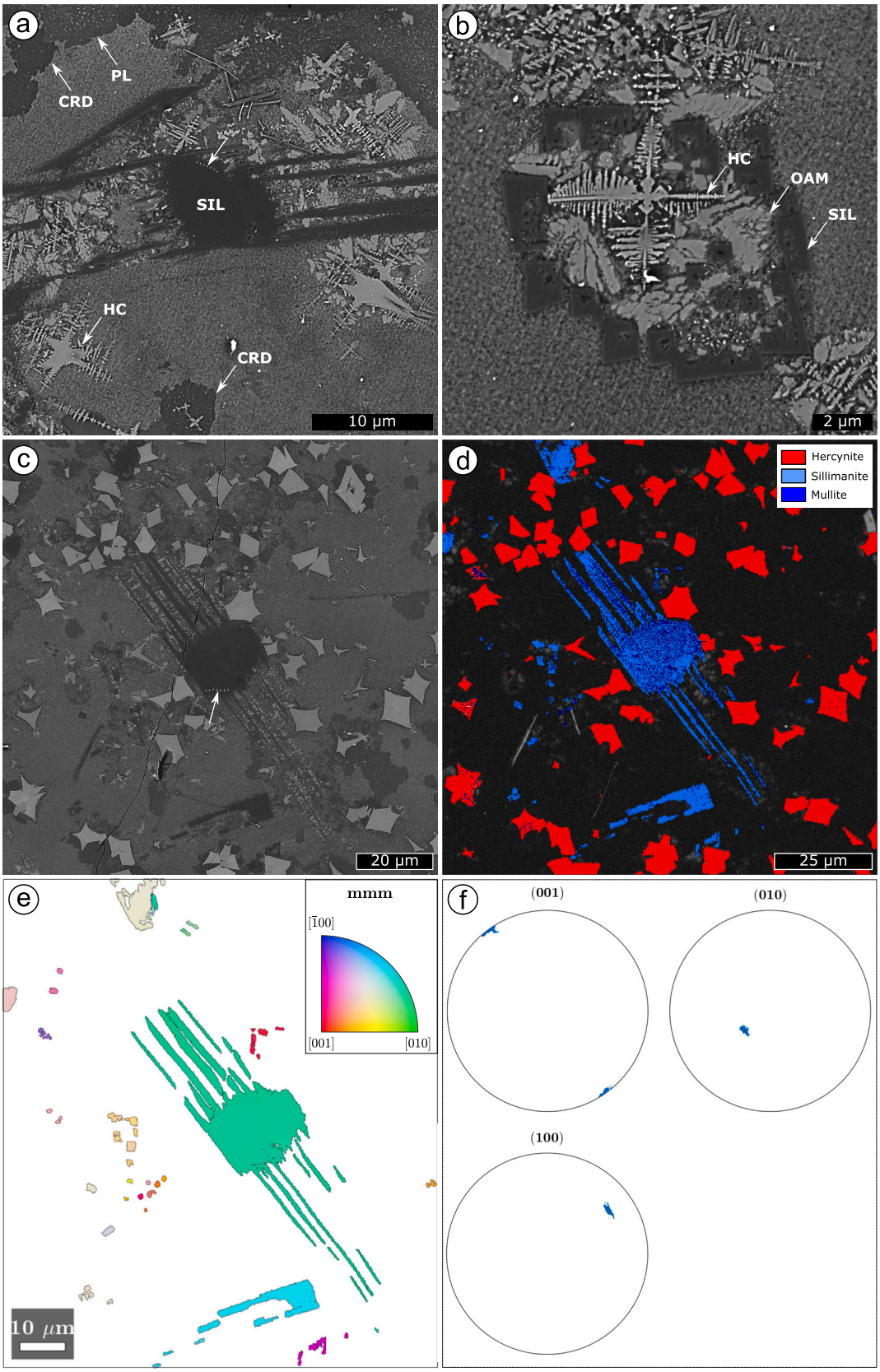

(caption on next page)

Fig. 4. Sillimanite microlites in the domain β of pst_1 (samples 18–06 and 20–02). (a) Longitudinal (subparallel to [001] crystallographic axis) section of sillimanite acicular microlites overgrowing a sillimanite clast (SIL). The boundary between clast and microlite is indicated by the white arrow and a short segment of it is highlighted by the white dotted line. Bright complex-shaped microlites are hercynite (HC). SEM-BSE image. (b) Section orthogonal to the long axis (corresponding to [001] axis) of acicular sillimanite microlites. Individual microlites have subparallel outer faces and internal hollow or maze-shaped geometry. Gray feathery microlites are orthoamphibole (OAM). SEM-BSE image. (c) Sillimanite acicular microlites, extending as opposite wings from a central sillimanite clast, and granular hercynite microlites. The boundary between the clast and the microlite is indicated by the white arrow and a short segment of it is highlighted by the white dotted line. SEM-BSE image. The EBSD map of this area is shown in (d)-(f). (d) EBSD phase map, showing hercynite (red colour) and sillimanite/mullite (blue colour) microlites, with band contrast image in the background. Notice that in the EBSD map the aluminosilicate is randomly indexed either as sillimanite (light blue) or mullite (dark blue). (e) Inverse pole figure map, colour-coded with respect to the Z direction, of sillimanite grains of (d). Mullite re-indexed as sillimanite. The largest grain in the centre of the map clearly shows a longitudinal section of acicular microlites overgrowing a sillimanite clast. The microlites grew in epitaxial continuity with the core clast. (f) Pole figures of the (100), (010), and (001) axes of the largest sillimanite grain. The pole figure of the (c)-axis (001) shows that the (001)-axis is parallel to the elongation of the acicular sillimanite microlites. (For interpretation of the references to colour in this figure legend, the reader is referred to the web version of this article).

pseudotachylyte, as strain-free flakes, aligned in the main host-rock foliation and arranged in decussate aggregates (Fig. 7c, e). Close to the pseudotachylyte vein these large flakes are pervasively deformed by fine kinking (Fig. 7d, f) as typically observed for many micas from other pseudotachylytes (Anderson et al., 2021; Bestmann et al., 2011, 2012).

4.3. Rb-Sr biotite ages

$^{87}Rb/^{87}Sr$ spot analyses of biotite in the pseudotachylyte host rock define two distinct populations. The pristine, undeformed granulite facies biotite defines an isochron with a date of 105.3 ± 4.1 Ma (s = 0.73) (Fig. 7a). Biotite flakes, adjacent to the pseudotachylyte, and affected by the pervasive fine kinking, define a younger date of 51.4 ± 5.1 Ma (s = 0.79) (Fig. 7b).

5. Discussion

5.1. Rb-Sr isochron ages of biotite in the pseudotachylyte host rock

The in-situ Rb-Sr data for pristine, undeformed granulite facies biotite is consistent with previously published ages (Del Moro et al., 2000). The data indicate that the Amaroni granulites cooled below 300–400 °C (approximate closure temperature of biotite: Armstrong et al., 1966; Verschure et al., 1980) since Lower Cretaceous time (105.3 ± 4.1 Ma) as already proposed by Schenk (1980, 1984, 1989). The pervasively kinked biotite in the host rock adjacent to the pseudotachylyte, associated with the coseismic rock damage (Fig. 7d, f), shows a reset, or partial reset, of its Rb-Sr systematics that defines a younger Rb-Sr isochron at 51.4 ± 5.1 Ma. This age is similar to that established for the pseudotachylyte-rich Curinga-Girifalco mylonitic thrust (43 ± 1 Ma: Schenk, 1980) that forms the sole of the Serre hanging wall block.

Although we do not speculate about the exact significance of this younger age, it seems reasonable to assume that pseudotachylyte formation postdates cooling below 300–400 °C and, therefore, is younger than ca. 105 Ma. Assuming that the 51.4 ± 5.1 Ma age records the age of pseudotachylyte formation, the most plausible interpretation is that the studied pseudotachylytes are Alpine in age, formed at shallow crustal levels, and are possibly related to the already known seismic activity of the *CGL* in the Eocene (Brandt and Schenk, 2020; Festa et al., 2020).

5.2. A model of cordierite growth and crystallisation of the pseudotachylyte

The quantitative interpretation of pseudotachylyte microstructures may benefit from available, experimental datasets for crystal growth within silicate melts quenched under controlled laboratory conditions. Here we use the Amaroni pseudotachylyte, for which shallow (base of the seismogenic continental crust) conditions of faulting have been established, to simulate the growth of cordierite microlites during quenching using crystal growth velocities determined in experiments for cordierite glasses. To this aim, we first model the cooling history of the frictional melt and then use this thermal evolution to simulate the cordierite grow. Constraints to thermal model are based on the geometry, microstructure and mineralogy of the pseudotachylyte as well as from the inferred ambient temperature of about 300 °C of faulting. This ambient temperature of faulting is assumed considering that (i) ca. 300 °C is almost univocally considered as the temperature for the transition from brittle fracturing to crystal plastic behaviour in quartz-bearing crustal rocks at common geological strain rates; (ii) pseudotachylytes are fault rocks typically developed close to the base of the brittle (seismogenic) crust; and (iii) the Rb-Sr biotite data indicate that the rocks had cooled to below 300–400 °C when the Amaroni pseudotachylytes were formed. In addition, literature datasets on thermal parameters of minerals involved in the frictional melting are used for modelling. The result of the simulation of cordierite growth during the quenching history is compared with the measured size of cordierite grains effectively present in the pseudotachylyte. Based on the observed microstructural relationships between the different microlites in the pseudotachylyte we reconstruct the sequence of crystallisation from the quenching frictional melt linked to the reconstructed cooling curve of the melt to the ambient host rock temperature (300 °C considering the shallow origin of seismic faulting as discussed above).

5.2.1. Cooling history of Amaroni pseudotachylytes

The cooling history of Amaroni pseudotachylyte is modelled for a vein thickness ranging from 0.5 to 2 cm, using the approach of Nielsen et al. (2008). The model considers that, during the fault slip episode, viscous shear of the melt vein is the main source of heating. Following Bestmann et al. (2012), we assume that the pseudotachylyte vein was generated during seismic slip that lasted 3 s with an average slip velocity $V = 1$ m/s. The assumed slip of 3 m likely overestimates the real slip, but this assumption does not significantly affect the temperature distribution inside the melt layer, given the steady-state conditions considered in the model.

The temperature $T(z)$ inside the melt, at a distance z from the vein centre, is (Nielsen et al., 2008):

$$T(z) = T_m - \left(\frac{W^2\eta_c}{8\kappa\rho c}\right) log_e \left(\frac{cosh^2\left(z\tau_{ss}\sqrt{V^2/W^2+1}\right)\Big/(\eta_c W)}{V^2/W^2+1} \right)$$

T_m, the melting temperature, is assumed to be 1300 °C, since host-rock garnet, biotite and feldspars should be completely melted at this temperature, while quartz and sillimanite would largely survive as clasts (Spray, 2010), as effectively observed in the Amaroni pseudotachylytes. The parameters W (characteristic velocity), η_c (viscosity) and τ_{ss} (shear stress) are taken from Nielsen et al. (2008). Thermal diffusivity κ, density ρ and heat capacity c were estimated, for a mixture of 65% melt and 35% clasts (quartz and sillimanite) at 1300 °C, using data from the literature (supplementary material).

At the solid/melt boundary $T = T_m$. In the host rock, the temperature at the time of slip arrest $T(\xi, t)$, where ξ is the distance from the solid/melt boundary, is (Nielsen et al., 2008):

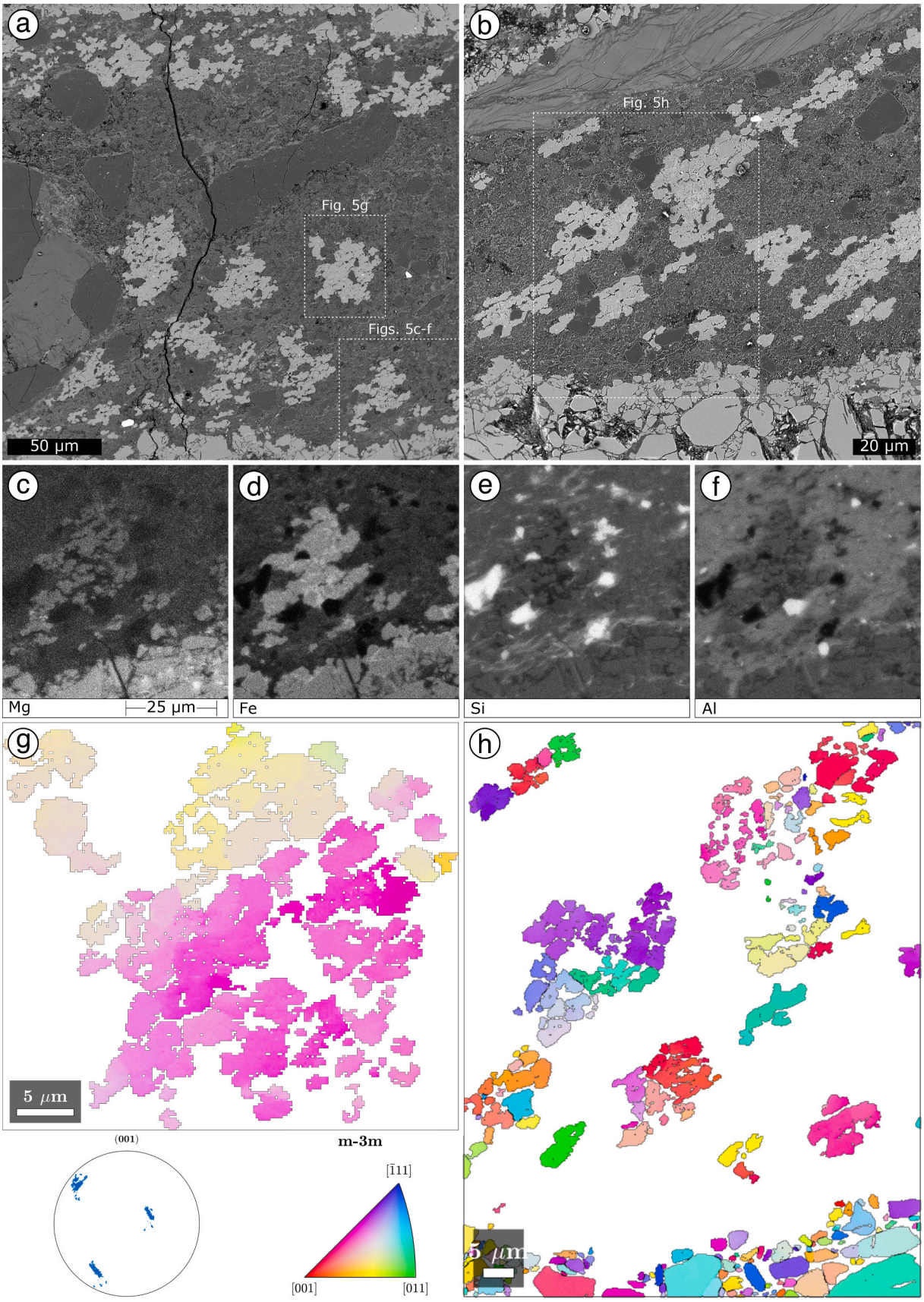

(caption on next page)

Fig. 5. Cauliflower garnet microlites across the injection vein of pst_2. (a) Overview of the pst_2 injection vein with a cluster of cauliflower garnet of increasing grain size toward the vein centre. The vein boundary, with intensely fragmented host rock garnet, is visible in the uppermost and lowermost part of the image. BSE image. (b) Same as the previous image, but with the cauliflower garnet with an elongate shape defining an flow fabric oblique to the vein boundaries marked by cataclastic host-rock garnet. BSE image. (c-f) EDS chemical element maps of the area outlined in Fig. 5a (dotted white square) of Mg (c), Fe (d), Si (e), and Al (f). The maps show the relative enrichment and depletion in these elements between the host-rock cataclastic garnet, the new garnet and the altered garnet; details are discussed in the main text; chemical analyses are available in the supplementary material. (g) EBSD inverse pole figure maps, colour coded with respect to the Z direction, of a garnet microlite (see location in (a)). Pole figure of the (001)-axis of garnet, showing that the 'cauliflower' is a single grain with only minor variations of the crystallographic orientation. (h) EBSD inverse pole figure maps, colour coded with respect to the Z direction, of elongated garnet microlites (see location in (a)). These elongated cauliflower garnets are clearly a cluster of grains with different crystallographic orientations. (For interpretation of the references to colour in this figure legend, the reader is referred to the web version of this article).

$$T(\xi,t) = T_i + \frac{T_m - T_i}{2}\left(erfc\left(\frac{\xi + vt}{2\sqrt{\kappa t}}\right) + e^{\frac{-\xi v}{\kappa}} erfc\left(\frac{\xi - vt}{2\sqrt{\kappa t}}\right)\right)$$

where T_i is the initial background temperature, v is the speed of migration of the melt/solid boundary and κ is the thermal diffusivity estimated for a mixture of 40% garnet, 40% quartz, 10% biotite and 10% sillimanite at T_i.

The evolution of T within and outside the vein after slip arrest is estimated by imposing the T profile at slip arrest as an initial condition to the heat conservation equation for purely conductive heat transport:

$$\frac{\partial T}{\partial t} = \kappa \Delta T$$

We assume that, immediately after the onset of cooling, the pseudotachylyte vein is composed of 45% melt, 20% spinel microlites and 35% clasts, based on XRPD analysis of sample 20–02. The latent heat of solidification of spinel microlites is neglected in the model, and the quenching of the remaining melt to glass is not associated to latent heat release. The temperature dependence of the thermal diffusivity of glass and minerals is considered in the model, using data from the literature (supplementary material). The result of the model for a background temperature of 300 °C is shown in Fig. 8.

In a melt cooling at the standard experimental cooling rate of 20 K/min, the transition from liquid to glass occurs at the glass transition temperature T_g, conventionally considered as the temperature at which the viscosity of the melt is $\sim 10^{13}$ Pa s (Richet and Bottinga, 1986). For a cordierite melt T_g is ~830 °C (Azín et al., 2005). If a melt is cooled more rapidly, the temperature at which the liquid structure is frozen into the glassy state (called fictive temperature T_f) is higher than T_g, and can be calculated as (Richet and Bottinga, 1986):

$$T_f = \left(log_e\left(q/q_0\right)\left(-R/E\right) + 1/T_g\right)^{-1}$$

where q is the cooling rate resulting from the model, q_0 is the reference cooling rate of 20 K/min, E is the activation energy for glass transition for a cordierite glass, and T_g is the glass transition temperature. For a cordierite glass quenched at the cooling rate of the Amaroni pseudotachylyte, the calculated T_f can be about 50 °C higher than the T_g.

5.2.2. Crystallisation of cordierite

Experimentally-derived growth velocity data for cordierite are applied to the cooling model of the Amaroni pseudotachylyte to investigate the likelihood of cordierite crystallisation (i) as a microlite, i.e. directly from the melt at temperatures between 900 and 1300 °C, or (ii) by devitrification at ambient conditions within the stability field of cordierite for metapelitic systems.

Cordierite has three polymorphs: (i) the hexagonal, high-T indialite (or α-cordierite); (ii) the orthorhombic low-temperature cordierite (or β-cordierite); and (iii) the metastable μ-cordierite, which is a solid solution with β-quartz structure. Cordierite microlites in quenched melts have been reported in natural pyrometamorphic rocks and paralavas (Balassone et al., 2004; Peretyazhko et al., 2018; Venkatesh, 1952). The cordierite polymorph formed in these cases is indialite, which crystallises with euhedral or skeletal morphology. During experimental crystallisation of cordierite glass, the first appearing polymorph is μ-cordierite, which subsequently transforms to indialite or cordierite. In these experiments, rapid nucleation and growth of crystals are only observed at temperatures well above 900 °C (e.g., Azín et al., 2005; Diaz-Mora et al., 2000; Fokin and Zanotto, 1999; Goel et al., 2007; Rudolph et al., 1993). Diaz-Mora et al. (2000) and Fokin and Zanotto (1999) described the morphology of cordierite crystals grown in glasses as either regular hexagonal or spherical/ellipsoidal shapes.

Rudolph et al. (1993), reported crystal growth velocities in cordierite glasses at temperatures between 900 and 1350 °C. Maximum velocities of up to 0.9 μm/s occur between 1200 and 1270 °C. These values, when applied to the cooling model of the Amaroni pseudotachylyte and considering a radial growth, are compatible with growth of cordierite globular-shaped crystals with a diameter of 5–10 μm in a few seconds when the melt temperature is between 900 and 1300 °C, irrespective of the background temperature in the host rock. According to Kitamura and Hiroi (1982), the transition between the stability fields of indialite and cordierite occurs at around 1000 °C for a cordierite with a Fe/(Mg + Fe) of 0.26. If spherulites crystallised from the melt at temperatures above 1000 °C, they probably formed as indialite and later transformed into low-temperature, orthorhombic cordierite at lower temperatures.

Fokin and Zanotto (1999) reported the growth velocity of μ-cordierite between 830 and 930 °C, i.e., around the glass transition for the pseudotachylyte melt. Using the data of Fokin and Zanotto (1999), we have estimated the potential growth of cordierite crystals in the cooling pseudotachylyte for different vein thicknesses and different background temperatures, in the case that cordierite crystallisation occurred by devitrification, i.e. below the glass transition temperature. The cooling rate of the pseudotachylyte vein is strongly dependent on the background temperature and the thickness of the vein. In the model, crystallisation of cordierite is allowed when the melt cools below T_f and is stopped when the temperature approaches 500 °C (the lower temperature bound for cordierite crystallisation: Seifert and Schreyer, 1970). Results are reported in Table 1 and the script used for calculations is available in the supplementary material. The analysis shows that significant growth of cordierite crystals by devitrification (e.g. crystals with a diameter of at least 1 μm) is not possible for background temperatures below 400 °C. In fact, if the background temperature is low (< 400 °C), and the vein is thin (< 2 cm), quenching is too fast and crystallisation of cordierite below the glass transition is hampered. Furthermore, this analysis might overestimate the growth of cordierite from the glass. In fact, Diaz-Mora et al. (2000) used a stoichiometric glass to crystallise μ-cordierite at 860 °C and 980 °C, and the crystal growth velocities measured are one order of magnitude slower than those reported by Fokin and Zanotto (1999) who used a TiO_2-rich glass to induce faster crystallisation.

The application of experimentally-derived growth velocities of cordierite crystals to the cooling model of the Amaroni pseudotachylyte confirms that cordierite crystallised directly from the melt during the short-lived, high-temperature transient at temperatures above 900 °C. Therefore, these cordierite microlites can give no information about the ambient temperature of pseudotachylyte formation.

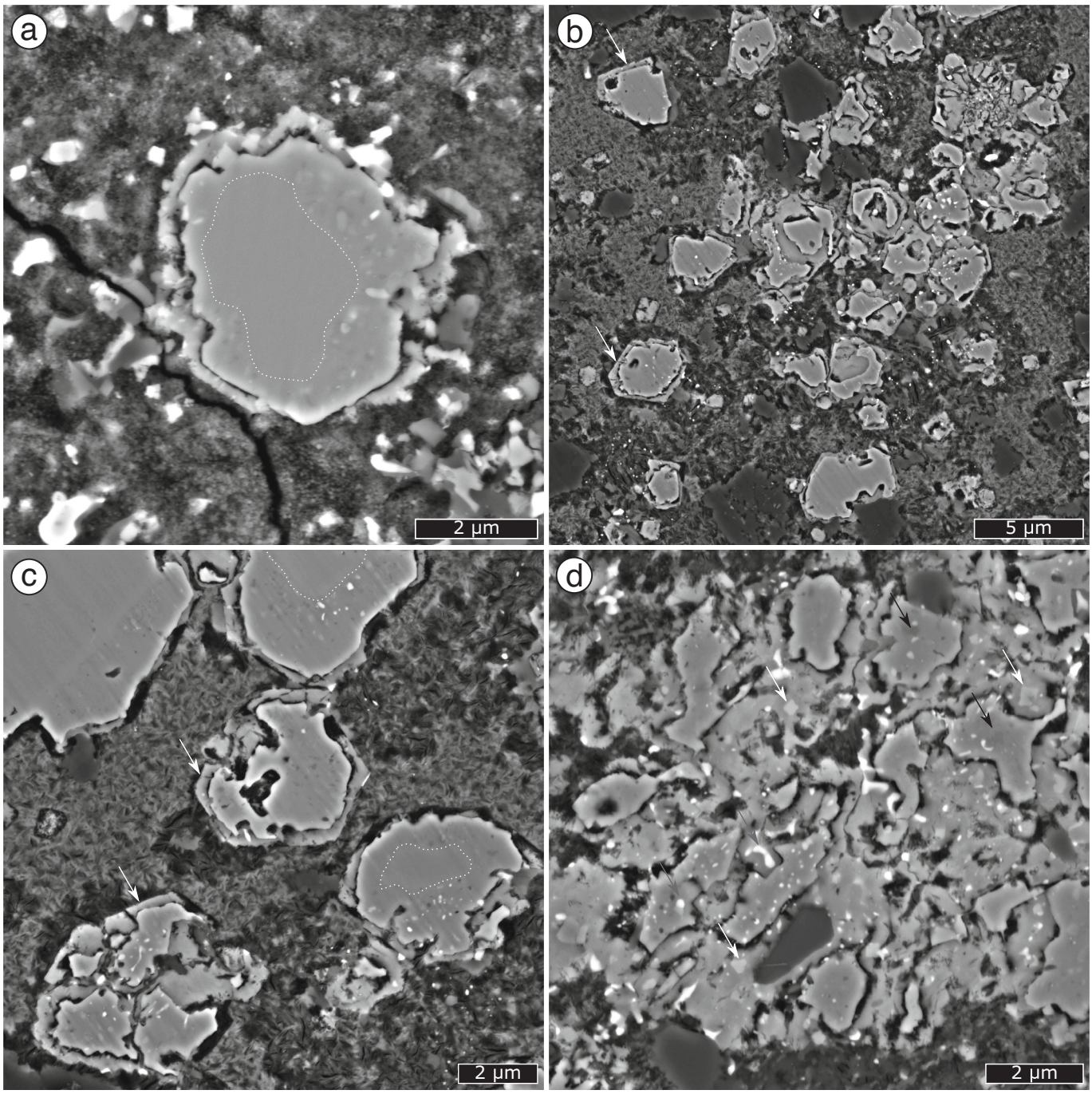

Fig. 6. Subhedral, corroded, small garnet microlites in pst_2. (a) Garnet microlite showing an inclusion-free core (encircled by the dotted white line) likely representing a seed garnet clast. The overgrowing garnet microlite, rich in inclusions, is surrounded by an alteration rim (likely Fe-chlorite), retaining the original idiomorphic shape of the microlite and the same kind of inclusions. (b-c) Clusters of garnet microlites showing the same features of that in (a). White arrows indicate locations where the alteration coronae still show perfectly plane crystal facets of the former garnet microlite. The white dotted lines in (c) encircle the inclusion-free cores of some microlites. (d) Detail of an altered garnet microlite with arrows indicating the three kind of inclusions described in the main text. All images are BSE images.

5.3. *Garnet 'cauliflower' microlites*

Garnet microlites with 'cauliflower' shape have been commonly reported in deep-seated pseudotachylytes (Altenberger et al., 2013; Austrheim and Boundy, 1994; Hawemann et al., 2018; Lund and Austrheim, 2003; Mancktelow et al., 2022; Pittarello et al., 2012). In the Amaroni pseudotachylytes, garnet cauliflowers are rare and only locally found in an injection vein. The rarity of garnet microlites likely reflects the disappearance of garnet clasts due to preferential comminution and melting in the pseudotachylyte melt (Papa et al., 2018). Since garnet 'cauliflowers' are commonly observed to overgrow garnet clasts (Pittarello et al., 2015), their nearly complete disappearance by melting could have hampered the growth of new microlitic garnet. Melting could have totally consumed garnet clasts in the fault vein that, conversely, could have locally survived in the thin injection vein where the melt temperature was probably lower and the high-temperature transient shorter.

The Fe-enrichment and Mg-depletion in garnet microlites with

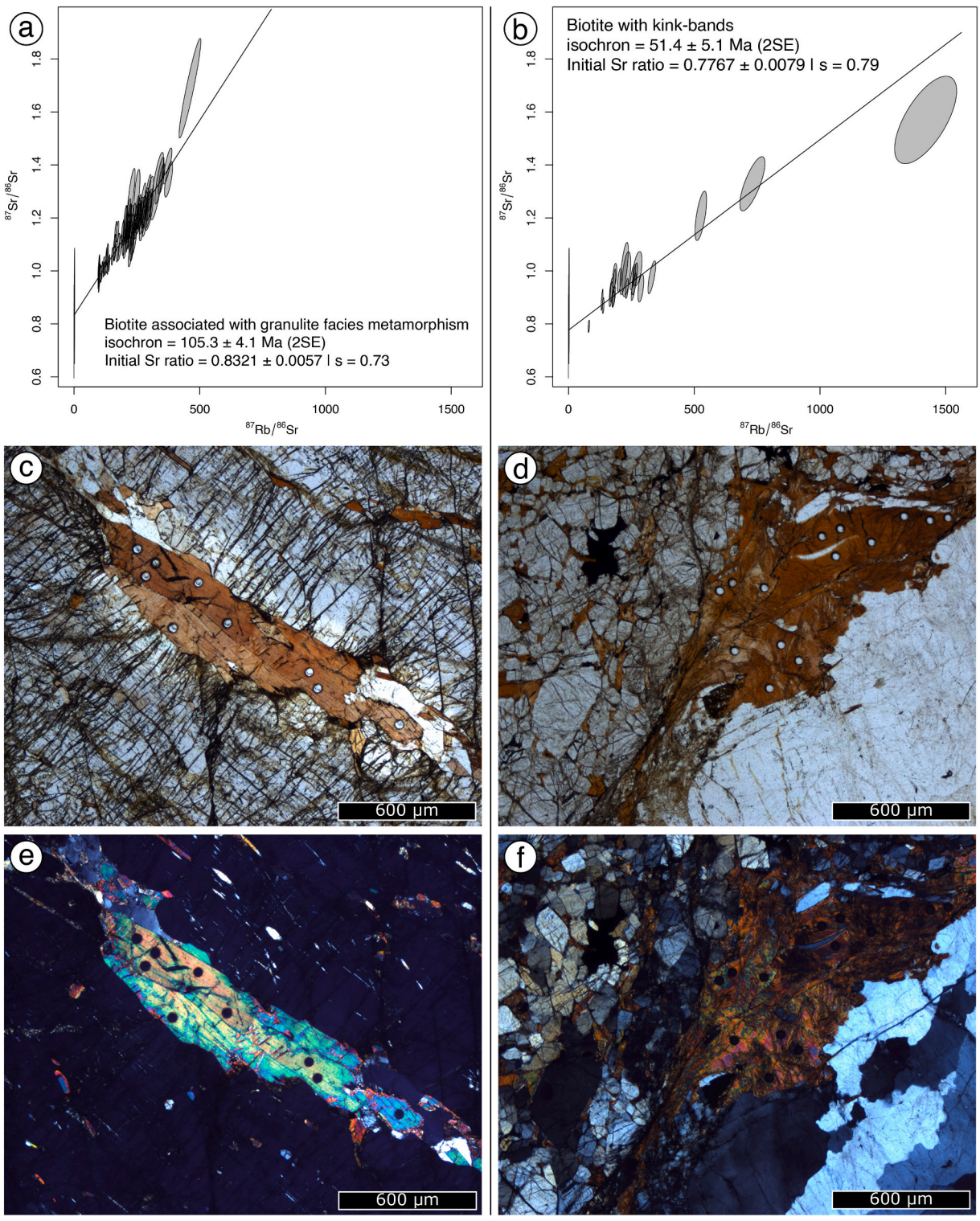

Fig. 7. Rb-Sr isochron plots for (a) undeformed granulite facies biotite and (b) biotite pervasively kinked during damage associated with pseudotachylyte. Plots are created using the ChrontouR package (Larson et al., 2023) for the open R scripting environment. The isochrons were calculated using the robust regression method of Powell (2020) where s = spine regression (see Powell (2020) for further explanation). Microstructures associated with the undeformed biotite are shown in (c) and (e), while those characterising the pervasively kinked biotite are shown in (d) and (f). Optical images in plane polarised light ((c) and (d)) and in cross polarised light ((e) and (f)).

respect to host-rock granulitic garnet observed in the Amaroni pseudotachylytes is a commonly reported feature (Altenberger et al., 2013; Austrheim et al., 1996; Pittarello et al., 2015). Altenberger et al. (2013), referring to experimental literature on magmatic garnet in mafic rocks (e.g. Green and Ringwood, 1968), concluded that crystallisation of Fe-rich garnets in Calabrian pseudotachylytes can be used to constrain a minimum ambient pressure of 0.7–0.8 GPa at the time of pseudotachylyte formation. For the Amaroni pseudotachylytes, this approximate pressure estimate can overlap with the highest pressure conditions at which cordierite can be stable and coexist with garnet (Hensen and

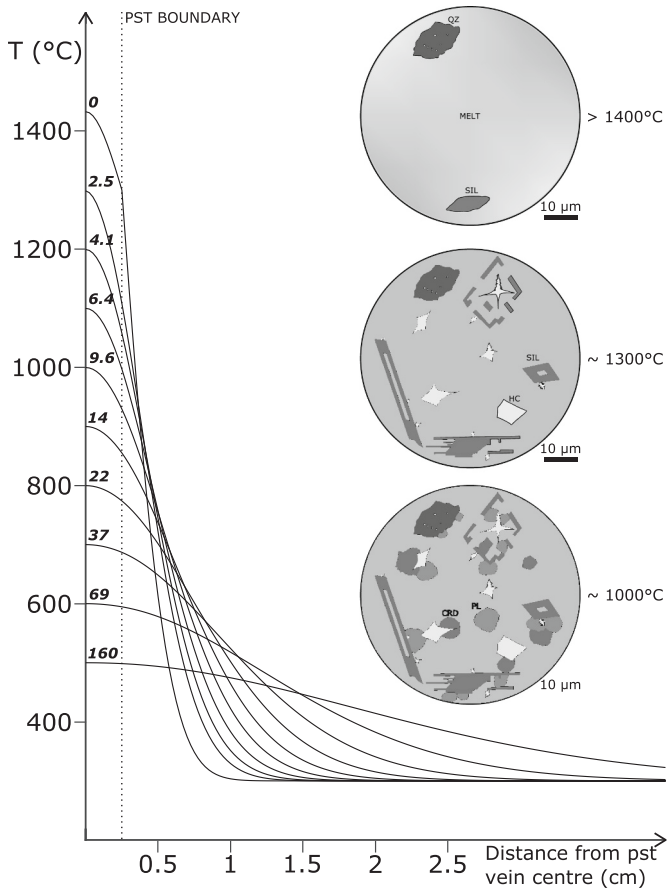

Fig. 8. Synoptic scheme for the development of the microlites of the Amaroni pseudotachylytes as a function of the temperature evolution of the frictional melt. The plot reports the calculated curves of temperature distribution across the vein and in the immediate host rock as a function of time from the start of melt quenching (time, in seconds, is shown by the number labels above the curves). Since the temperature distribution is symmetrical with respect to the centre of the pseudotachylyte vein, only a half is shown and the temperature axis is drawn in the middle of the vein. The dotted vertical line represents the pseudotachylyte boundary for the considered vein thickness of 0.5 cm. The images in the circles represent the microstructures developed at decreasing temperatures: > 1400 °C (frictional melt including survived clasts of quartz and sillimanite); ca. 1300 °C (melt including sillimanite microlites, nucleated epitaxially on sillimanite clasts, and hercynite microlites); and ca. 1000 °C (after crystallisation of cordierite and plagioclase).

Green, 1973). However, Mn-rich garnet can be stable in peraluminous silicic melts down to pressures lower than 0.3 GPa (Green, 1977). In the Amaroni pseudotachylytes, garnet microlites are slightly enriched in Mn and this might have expanded the garnet stability field to pressures lower than 0.7–0.8 GPa.

The dendritic shape and the decrease in size and increase in abundance toward the vein boundary are clear evidence that garnet microlites crystallised directly from the melt (e.g. Clerc et al., 2018). This means that they crystallised during the high-temperature transient and therefore they can give no information on ambient temperature. Zhong et al. (2021) suggested that frictional melts can be highly overpressured, showing that the pressure recorded by quartz inclusions in dendritic garnets that grew from frictional melts are 0.5 GPa higher than the estimated ambient pressure. This finding casts doubts on the robustness of considering garnet 'cauliflowers' as indicators of high ambient pressure, since they may record the transient overpressure in the frictional melt.

In the Amaroni pseudotachylytes, garnet was undoubtedly transiently stable as it grew in the melt and locally developed crystal facets

Table 1
Modelling results of pseudotachylyte-melt cooling and of cordierite microlite growth as a function of the vein thickness and background temperature. (a) Maximum growth diametre of μ-cordierite crystals calculated, for the cooling model of the Amaroni pseudotachylyte, based on the data from Fokin and Zanotto (1999). Using the data for α-cordierite, the calculated growth is always smaller than 0.1 μm. (b) Timeframes over which the pseudotachylyte vein cools below 500 °C.

	Background temperature		
Pst thickness	300 °C	350 °C	400 °C
0.5 cm	0.05 μm	0.06 μm	0.09 μm
1 cm	0.10 μm	0.13 μm	0.20 μm
1.5 cm	0.17 μm	0.23 μm	0.36 μm
2 cm	0.26 μm	0.36 μm	0.57 μm

	Background temperature		
Pst thickness	300 °C	350 °C	400 °C
0.5 cm	165 s	250 s	487 s
1 cm	403 s	619 s	1214 s
1.5 cm	746 s	1152 s	2269 s
2 cm	1194 s	1851 s	3655 s

(Fig. 6b-d). However, our study strongly suggests that Amaroni pseudotachylytes formed at shallow-crustal conditions, highlighting that any interpretation on ambient conditions during pseudotachylyte formation based on garnet growth in the cooling melt must be carefully pondered.

5.4. Order of crystallisation of microlites

The shape of microlites (from skeletal to dendritic and feathery) indicates nucleation and growth from melt at undercooling conditions (Lofgren, 1974). In the pseudotachylyte melt, hercynite, sillimanite, and ortho-amphibole nucleated and grew within a few seconds, aided by fast diffusion at high temperatures. The distribution of different microlites into layers resulted from the heterogeneous composition of the melts, derived from melting of different host-rock minerals, incomplete mixing of these melts and melt deformation by flow.

The hercynite-rich layers reflect the Fe- and Al-rich composition of the melt and the ease of nucleation of Fe-oxides due to their high entropy change with melting (Carmichael et al., 1974). Hercynite microlites were probably the first to crystallise from the quenching melt. Alternatively, hercynite microlites crystallised by incongruent melting of garnet breaking down to spinel + glass due to fast shock-melting (Stähle, 1975). In both cases, given the extremely fast cooling rate, the microlites were 'frozen' within the quenched glass in a matter of a few seconds. The shape of the microlites is controlled by the degree of undercooling (e.g. Lofgren, 1974). For hercynite microlites a change in shape from granular, and coarser, to dendritic is observed. The dendritic microlites nucleated heterogeneously over sillimanite microlites.

Sillimanite microlites are much less abundant and unevenly distributed than hercynite. They only occur in domain β, where hercynite microlites are more scattered, and crystallised by heterogeneous nucleation on sillimanite clasts before hercynite.

Hercynite, ortho-amphibole, and high-T aluminosilicates (sillimanite and mullite) microlites have been observed in pseudotachylytes within metapelites in a large range of pressure/temperature conditions (ortho-amphibole: Magloughlin, 1989, and Ray, 2004; hercynite: e.g. Menant et al., 2018, and Sarkar and Chattopadhyay, 2019; sillimanite: Altenberger et al., 2013; mullite: Moecher and Brearley, 2004, and Ujiie et al., 2007). All these microlites reflect the high-T transient during the frictional melting and melt quenching, and give no information on the ambient pressure and temperature of pseudotachylyte formation.

Considering (i) the thermal model of the Amaroni pseudotachylyte fault vein, (ii) the observed microstructural relationships between the

different microlites, and (iii) the calculated conditions of cordierite growth, we infer the following sequence of events from the initial development of the frictional melt (as illustrated in Fig. 8): (1) development of melt with $T_m > 1400$ °C that allowed survival of sillimanite and quartz clasts and almost complete disappearance of garnet, biotite and feldspar clast; (2) growth of hercynite and sillimanite – this latter overgrowing epitaxially sillimanite clast seeds – at $T \sim 1300$ °C; (3) initial growth of spheroidal-shaped microlites of cordierite and plagioclase at $T < 1300$ °C.

6. Conclusions

We applied a novel approach consisting in Rb-Sr dating of biotite pervasively kinked in the seismically damaged fault zone and of undeformed host rock biotite to constrain the formation conditions of pristine pseudotachylytes hosted in lower-crustal granulites in the Serre Massif of Calabria. Our new geochronological data suggest that pseudotachylytes formed by shallow seismic faulting after the rocks had cooled below ca. 300–400 °C, possibly related to the already known seismic activity of the Curinga-Girifalco Line in the Eocene.

The studied pseudotachylyte contains sillimanite and hercynite microlites, and garnet, plagioclase and cordierite poikilitic grains. Considering the shallow level of seismic faulting, we infer that all these minerals crystallised during the transient high temperature stages of melt quenching.

We also present a calibrated model of pseudotachylyte quenching and calculate the final size of the crystallising cordierite grains on the basis of available experimental datasets on growth of cordierite crystals from a quenching melt. The match between the observed and calculated size of cordierite grains legitimates extrapolation of experimental data to natural systems and indicates the reliability of the thermal modelling of pseudotachylyte melt quenching. The results of our modelling and microstructural observations, integrated with literature information, allow the reconstruction of the sequence of mineral crystallisation to be linked with the thermal history of quenching of the pseudotachylyte melt. Our analysis highlights the ambiguity of the significance of garnet microlites in pristine pseudotachylytes that, in the present case, cannot be used as a proxy for a deep-seated origin of the pseudotachylytes.

Declaration of Competing Interest

The authors declare that they have no known competing financial interests or personal relationships that could have appeared to influence the work reported in this paper.

Acknowledgement

We acknowledge the assistance of: Federico Zorzi and Marco Favero for XRPD; Jacopo Nava for SEM analysis; Leonardo Tauro for thin section preparation; Stefano Castelli for samples photography; Mark Button for Rb-Sr analytical support. The research was supported by funding from Alfredo Camacho, from the University of Padova, and from project PRIN 2020WPMFE9 “THALES” (PI: Giorgio Pennacchioni). We sincerely appreciate valuable comments and suggestions, as well as constructive criticism, by Volker Schenk and two anonymous reviewers, which helped us in improving the quality of the manuscript.

Appendix A. Supplementary data

Supplementary data to this article can be found online at https://doi.org/10.1016/j.lithos.2023.107375.

References

Acquafredda, P., Fornelli, A., Paglionico, A., Piccarreta, G., 2006. Petrological evidence for crustal thickening and extension in the Serre granulite terrane (Calabria, southern Italy). Geol. Mag. 143 (2), 145–163. https://doi.org/10.1017/S0016756805001482.

Acquafredda, P., Fornelli, A., Piccarreta, G., Pascazio, A., 2008. Multi-stage dehydration-decompression in the metagabbros from the lower crustal rocks of the Serre (southern Calabria, Italy). Geol. Mag. 145 (3), 397–411. https://doi.org/10.1017/S001675680700430X.

Altenberger, U., Prosser, G., Grande, A., Günter, C., Langone, A., 2013. A seismogenic zone in the deep crust indicated by pseudotachylytes and ultramylonites in granulite-facies rocks of Calabria (Southern Italy). Contrib. Mineral. Petrol. 166 (4), 975–994. https://doi.org/10.1007/s00410-013-0904-3.

Anderson, E.K., Song, W.J., Johnson, S.E., Cruz-Uribe, A.M., 2021. Mica kink-band geometry as an indicator of coseismic dynamic loading. Earth Planet. Sci. Lett. 567, 117000. https://doi.org/10.1016/j.epsl.2021.117000.

Armstrong, R.L., Jäger, E., Eberhardt, P., 1966. A comparison of K-Ar and Rb-Sr ages on Alpine biotites. Earth Planet. Sci. Lett. 1 (1), 13–19. https://doi.org/10.1016/0012-821X(66)90097-5.

Austrheim, H., 1987. Eclogitization of lower crustal granulites by fluid migration through shear zones. Earth Planet. Sci. Lett. 81, 221–232. https://doi.org/10.1016/0012-821X(87)90158-0.

Austrheim, H., Boundy, T.M., 1994. Pseudotachylytes generated during seismic faulting and eclogitization of the deep crust. Science 265 (5168), 82–83.

Austrheim, H., Dunkel, K.G., Plümper, O., Ildefonse, B., Liu, Y., Jamtveit, B., 2017. Fragmentation of wall rock garnets during deep crustal earthquakes. Sci. Adv. 3 (2) https://doi.org/10.1126/sciadv.1602067.

Austrheim, H., Erambert, M., Boundy, T.M., 1996. Garnets recording deep crustal earthquakes. Earth Planet. Sci. Lett. 139, 223–238.

Azín, N.J., Camerucci, M.A., Cavalieri, A.L., 2005. Crystallisation of non-stoichiometric cordierite glasses. Ceram. Int. 31 (1), 189–195. https://doi.org/10.1016/j.ceramint.2004.04.002.

Balassone, G., Franco, E., Mattia, C.A., Puliti, R., 2004. Indialite in xenolithic rocks from Somma-Vesuvius volcano (Southern Italy): Crystal chemistry and petrogenetic features. Am. Mineral. 89 (1), 1–6. https://doi.org/10.2138/am-2004-0101.

Beeler, N.M., Di Toro, G., Nielsen, S., 2016. Earthquake source properties from pseudotachylyte. Bull. Seismol. Soc. Am. 106 (6), 2764–2776. https://doi.org/10.1785/0120150344.

Bestmann, M., Pennacchioni, G., Frank, G., Göken, M., de Wall, H., 2011. Pseudotachylyte in muscovite-bearing quartzite: Coseismic friction-induced melting and plastic deformation of quartz. J. Struct. Geol. 33 (2), 169–186. https://doi.org/10.1016/j.jsg.2010.10.009.

Bestmann, M., Pennacchioni, G., Nielsen, S., Göken, M., de Wall, H., 2012. Deformation and ultrafine dynamic recrystallization of quartz in pseudotachylyte-bearing brittle faults: a matter of a few seconds. J. Struct. Geol. 38, 21–38. https://doi.org/10.1016/j.jsg.2011.10.001.

Brandt, S., Schenk, V., 2020. Metamorphic response to Alpine thrusting of a crustal-scale basement nappe in southern Calabria (Italy). J. Petrol. https://doi.org/10.1093/petrology/egaa063.

Brückner, L.M., Trepmann, C.A., 2021. Stresses during pseudotachylyte formation - evidence from deformed amphibole and quartz in fault rocks from the Silvretta basal thrust (Austria). Tectonophysics 817 (June). https://doi.org/10.1016/j.tecto.2021.229046.

Caggianelli, A., Prosser, G., Del Moro, A., 2000. Cooling and exhumation history of deep-seated and shallow level, late Hercynian granitoids from Calabria. Geol. J. 35 (1), 33–42. https://doi.org/10.1002/(SICI)1099-1034(200001/03)35:1<33::AID-GJ836>3.0.CO;2-U.

Caggianelli, A., Prosser, G., Festa, V., Langone, A., Spiess, R., 2013. From the upper to the lower continental crust exposed in Calabria. Geol. Field Trips 5 (1.2), 1–49. https://doi.org/10.3301/gft.2013.02.

Campbell, L., Menegon, L., 2022. High stress deformation and short-term thermal pulse preserved in pyroxene microstructures from exhumed lower crustal seismogenic faults (Lofoten, Norway) Journal of Geophysical Research: Solid Earth. J. Geophys. Res. Solid Earth, e2021JB023, 1–25. https://doi.org/10.1029/2021JB023616.

Campbell, L.R., Menegon, L., Fagereng, Å., Pennacchioni, G., 2020. Earthquake nucleation in the lower crust by local stress amplification. Nat. Commun. 11 (1), 1–9. https://doi.org/10.1038/s41467-020-15150-x.

Carmichael, I.S.E., Turner, F.J., Verhoogen, J., 1974. Igneous Petrology. McGraw-Hill, New York. https://doi.org/10.1017/s0016756800046318.

Clerc, A., Renard, F., Austrheim, H., Jamtveit, B., 2018. Spatial and size distributions of garnets grown in a pseudotachylyte generated during a lower crust earthquake. Tectonophysics 733 (July 2017), 159–170. https://doi.org/10.1016/j.tecto.2018.02.014.

Del Moro, A., Fornelli, A., Piccarreta, G., 2000. Tectonothermal history of the Hercynian continental crust of the Serre (Southern Calabria, Italy) monitored by Rb-Sr biotite resetting. Terra Nova 12 (5), 239–244. https://doi.org/10.1046/j.1365-3121.2000.00304.x.

Del Moro, A., Paglionico, A., Piccarreta, G., Rottura, A., 1986. Tectonic structure and post-Hercynian evolution of the Serre, Calabrian Arc, southern Italy: geological, petrological and radiometric evidences. Tectonophysics 124 (3–4), 223–238. https://doi.org/10.1016/0040-1951(86)90202-7.

Di Toro, G., Pennacchioni, G., Teza, G., 2005a. Can pseudotachylytes be used to infer earthquake source parameters? An example of limitations in the study of exhumed faults. Tectonophysics 402 (1–4), 3–20. https://doi.org/10.1016/j.tecto.2004.10.014.

Di Toro, G., Nielsen, S., Pennacchioni, G., 2005b. Earthquake rupture dynamics frozen in exhumed ancient faults. Nature 436 (7053), 1009–1012. https://doi.org/10.1038/nature03910.

Diaz-Mora, N., Zanotto, E.D., Hergt, R., Müller, R., 2000. Surface crystallization and texture in cordierite glasses. J. Non-Cryst. Solids 273 (1–3), 81–93. https://doi.org/10.1016/S0022-3093(00)00147-2.

Dunkel, K.G., Morales, L.F.G., Jamtveit, B., 2021. Pristine microstructures in pseudotachylytes formed in dry lower crust, Lofoten, Norway Subject Areas: Author for correspondence. In: Philosophical Transactions of the Royal Society A: Mathematical, Physical and Engineering Sciences.

Dunkel, K.G., Zhong, X., Arnestad, P.F., Valen, L.V., Jamtveit, B., 2020. High transient stress in the lower crust: evidence from dry pseudotachylytes in granulites, Lofoten Archipelago, northern Norway. Geol. September. https://doi.org/10.1130/g48002.1.

Festa, V., Cicala, M., Tursi, F., 2020. The Curinga–Girifalco Line in the framework of the tectonic evolution of the remnant Alpine chain in Calabria (southern Italy). Int. J. Earth Sci. 109 (7), 2583–2598. https://doi.org/10.1007/s00531-020-01918-5.

Festa, V., Fornelli, A., Paglionico, A., Pascazio, A., Piccarreta, G., Spiess, R., 2012. Asynchronous extension of the late-Hercynian crust in Calabria. Tectonophysics 518–521, 29–43. https://doi.org/10.1016/j.tecto.2011.11.007.

Fokin, V.M., Zanotto, E.D., 1999. Surface and volume nucleation and growth in TiO2-cordierite glasses. J. Non-Cryst. Solids 246 (1), 115–127. https://doi.org/10.1016/S0022-3093(99)00007-1.

Fondriest, M., Mecklenburgh, J., Passelègue, F.X., Artioli, G., Nestola, F., Spagnuolo, E., Rempe, M., Di Toro, G., 2020. Pseudotachylyte alteration and the rapid fade of Earthquake scars from the geological record. Geophys. Res. Lett. 47 (22), 1–9. https://doi.org/10.1029/2020GL090020.

Fornelli, A., Piccarreta, G., Del Moro, A., Acquafredda, P., 2002. Multi-stage melting in the lower crust of the Serre (southern Italy). J. Petrol. 43 (12), 2191–2217. https://doi.org/10.1093/petrology/43.12.2191.

Goel, A., Shaaban, E.R., Melo, F.C.L., Ribeiro, M.J., Ferreira, J.M.F., 2007. Non-isothermal crystallization kinetic studies on MgO-Al2O3-SiO2-TiO2 glass. J. Non-Cryst. Solids 353 (24–25), 2383–2391. https://doi.org/10.1016/j.jnoncrysol.2007.04.008.

Green, T.H., 1977. Garnet in silicic liquids and its possible use as a P-T indicator. Contrib. Mineral. Petrol. 65 (1), 59–67. https://doi.org/10.1007/BF00373571.

Green, Trevor H., Ringwood, A.E., 1968. Origin of garnet phenocrysts in calc-alkaline rocks. Contrib. Mineral. Petrol. 18 (2), 163–174. https://doi.org/10.1007/BF00371807.

Hawemann, F., Mancktelow, N.S., Wex, S., Camacho, A., Pennacchioni, G., 2018. Pseudotachylyte as field evidence for lower-crustal earthquakes during the intracontinental Petermann Orogeny (Musgrave Block, Central Australia). Solid Earth 9 (3), 629–648. https://doi.org/10.5194/se-9-629-2018.

Hensen, B.J., Green, D.H., 1973. Experimental study of the stability of cordierite and garnet in pelitic compositions at high pressures and temperatures - III. Synthesis of experimental data and geological applications. Contrib. Mineral. Petrol. 38 (2), 151–166. https://doi.org/10.1007/BF00373879.

Hogmalm, K.J., Zack, T., Karlsson, A.K.O., Sjöqvist, A.S.L., Garbe-Schönberg, D., 2017. In situ Rb-Sr and K-Ca dating by LA-ICP-MS/MS: an evaluation of N2O and SF6 as reaction gases. J. Anal. At. Spectrom. 32 (2), 305–313. https://doi.org/10.1039/c6ja00362a.

Jackson, J., Austrheim, H., McKenzie, D., Priestley, K., 2004. Metastability, mechanical strength, and the support of mountain belts. Geology 32 (7), 625–628. https://doi.org/10.1130/G20397.1.

Johnson, S.E., Song, W.J., Vel, S.S., Song, B.R., Gerbi, C.C., 2021. Energy partitioning, dynamic fragmentation, and off-fault damage in the earthquake source volume. J. Geophys. Res. Solid Earth 126 (11), 1–40. https://doi.org/10.1029/2021JB022616.

Kirkpatrick, J.D., Rowe, C.D., 2013. Disappearing ink: how pseudotachylytes are lost from the rock record. J. Struct. Geol. 52 (1), 183–198. https://doi.org/10.1016/j.jsg.2013.03.003.

Kitamura, M., Hiroi, Y., 1982. Contributions to mineralogy and petrology indialite from Unazuki Pelitic Schist, Japan, and its transition texture to Cordierite. Contrib. Mineral. Petrol. 80, 110–116.

Kruhl, J.H., Huntemann, T., 1991. The structural state of the former lower continental crust in Calabria (S. Italy). Geol. Rundsch. 80 (2), 289–302. https://doi.org/10.1007/BF01829367.

Langone, A., Gueguen, E., Prosser, G., Caggianelli, A., Rottura, A., 2006. The Curinga-Girifalco fault zone (northern Serre, Calabria) and its significance within the Alpine tectonic evolution of the western Mediterranean. J. Geodyn. 42 (4–5), 140–158. https://doi.org/10.1016/j.jog.2006.06.004.

Larson, K.P., Button, M., Shrestha, S., Camacho, A., 2023. A comparison of 87Rb/87Sr and 40Ar/39Ar dates: evaluating the problem of excess 40Ar in Himalayan mica. Earth Planet. Sci. Lett. 609, 118058. https://doi.org/10.1016/j.epsl.2023.118058.

Lazari, F., Castagna, A., Nielsen, S., Griffith, A., Pennacchioni, G., Gomila, R., Resor, P., Cornelio, C., Di Toro, G., 2023. Frictional power dissipation in a seismic ancient fault. Earth Planet. Sci. Lett. 607, 118057. https://researchdata.cab.unipd.it/id/eprint/725.

Lofgren, G.E., 1974. An experimental study of plagioclase crystal morphology; isothermal crystallization. Am. J. Sci. 274 (3), 243–273. https://doi.org/10.2475/ajs.274.3.243.

Lund, M.G., Austrheim, H., 2003. High-pressure metamorphism and deep-crustal seismicity: evidence from contemporaneous formation of pseudotachylytes and eclogite facies coronas. Tectonophysics 372 (1–2), 59–83. https://doi.org/10.1016/S0040-1951(03)00232-4.

Magloughlin, J.F., 1989. The nature and significance of pseudotachylite from the Nason terrane, North Cascade Mountains, Washington. J. Struct. Geol. 11 (7), 907–917. https://doi.org/10.1016/0191-8141(89)90107-7.

Magloughlin, J.F., 2005. Immiscible sulfide droplets in pseudotachylyte: evidence for high temperature (> 1200 °C) melts. Tectonophysics 402 (1–4 SPEC. ISS), 81–91. https://doi.org/10.1016/j.tecto.2004.11.011.

Mancktelow, N.S., Camacho, A., Pennacchioni, G., 2022. Time-lapse record of an earthquake in the Dry Felsic lower Continental Crust preserved in a Pseudotachylyte-Bearing Fault. J. Geophys. Res. Solid Earth 127 (4), 1–32. https://doi.org/10.1029/2021JB022878.

Menant, A., Angiboust, S., Monié, P., Oncken, O., Guigner, J.M., 2018. Brittle deformation during Alpine basal accretion and the origin of seismicity nests above the subduction interface. Earth Planet. Sci. Lett. 487, 84–93. https://doi.org/10.1016/j.epsl.2018.01.029.

Menegon, L., Pennacchioni, G., Malaspina, N., Harris, K., Wood, E., 2017. Earthquakes as Precursors of Ductile Shear zones in the dry and strong lower Crust. Geochem. Geophys. Geosyst. 18 (12), 4356–4374. https://doi.org/10.1002/2017GC007189.

Moecher, D.P., Brearley, A.J., 2004. Mineralogy and petrology of a mullite-bearing pseudotachylyte: Constraints on the temperature of coseismic frictional fusion. Am. Mineral. 89 (10), 1486–1495. https://doi.org/10.2138/am-2004-1017.

Nielsen, S., Di Toro, G., Hirose, T., Shimamoto, T., 2008. Frictional melt and seismic slip. J. Geophys. Res. Solid Earth 113 (1), 1–20. https://doi.org/10.1029/2007JB005122.

Papa, S., Pennacchioni, G., Angel, R.J., Faccenda, M., 2018. The fate of garnet during (deep-seated) coseismic frictional heating: the role of thermal shock. Geology 46 (5). https://doi.org/10.1130/G40077.1.

Pennacchioni, G., Scambelluri, M., Bestmann, M., Notini, L., Nimis, P., Plümper, O., Faccenda, M., Nestola, F., 2020. Record of intermediate-depth subduction seismicity in a dry slab from an exhumed ophiolite. Earth Planet. Sci. Lett. 548, 116490. https://doi.org/10.1016/j.epsl.2020.116490.

Peretyazhko, I.S., Savina, E.A., Khromova, E.A., Karmanov, N.S., Ivanov, A.V., 2018. Unique Clinkers and Paralavas from a New Nyalga combustion metamorphic complex in Central Mongolia: mineralogy, geochemistry, and genesis. Petrology 26 (2). https://doi.org/10.1134/S0869591118020054.

Petley-Ragan, A., Ben-Zion, Y., Austrheim, H., Ildefonse, B., Renard, F., Jamtveit, B., 2019. Dynamic earthquake rupture in the lower crust. Sci. Adv. 5 (7) https://doi.org/10.1126/sciadv.aaw0913.

Pittarello, L., Di Toro, G., Bizzarri, A., Pennacchioni, G., Hadizadeh, J., Cocco, M., 2008. Energy partitioning during seismic slip in pseudotachylyte-bearing faults (Gole Larghe Fault, Adamello, Italy). Earth Planet. Sci. Lett. 269 (1–2), 131–139. https://doi.org/10.1016/j.epsl.2008.01.052.

Pittarello, L., Habler, G., Abart, R., Rhede, D., 2015. Garnet growth in frictional melts of the Ivrea Zone (Italy). Ital. J. Geosci. 134 (1), 149–161. https://doi.org/10.3301/IJG.2014.53.

Pittarello, L., Pennacchioni, G., Di Toro, G., 2012. Amphibolite-facies pseudotachylytes in Premosello metagabbro and felsic mylonites (Ivrea Zone, Italy). Tectonophysics 580, 43–57. https://doi.org/10.1016/j.tecto.2012.08.001.

Powell, D., 2020. Quantile Treatment Effects in the Presence of Covariates. Rev. Econ. Stat. 102 (5), 994–1005. https://doi.org/10.1162/rest_a_00858.

Ray, S.K., 2004. Melt - Clast interaction and power-law size distribution of clasts in pseudotachylytes. J. Struct. Geol. 26 (10), 1831–1843. https://doi.org/10.1016/j.jsg.2004.02.009.

Redaa, A., Farkaš, J., Gilbert, S., Collins, A.S., Wade, B., Löhr, S., Zack, T., Schönberg, D., 2021. Assessment of elemental fractionation and matrix effects during in situ Rb–Sr dating of phlogopite by LA-ICP-MS/MS: implications for the accuracy and precision of mineral ages. J. Anal. At. Spectrom. 36, 322–344. https://doi.org/10.1039/D0JA00299B.JAAS.

Richet, P., Bottinga, Y., 1986. Thermochemical Properties of Silicate Glasses and Liquids: a Review. Rev. Geophys. 24 (1), 1–25.

Rösel, D., Zack, T., 2022. LA-ICP-MS/MS Single-Spot Rb-Sr dating. Geostand. Geoanal. Res. 46 (2), 143–168. https://doi.org/10.1111/ggr.12414.

Rudolph, T., Pannhorst, W., Petzow, G., 1993. Determination of activation energies for the crystallization of a cordierite-type glass. J. Non-Cryst. Solids 155 (3), 273–281. https://doi.org/10.1016/0022-3093(93)91262-2.

Sarkar, A., Chattopadhyay, A., 2019. Microstructure and geochemistry of pseudotachylyte veins from Sarwar-Junia Fault Zone, India: Implications for frictional melting process in a seismic fault zone. Geol. J. Septemb. 2020, 1–29. https://doi.org/10.1002/gj.3900.

Schenk, V., 1980. U-Pb and Rb-Sr Radiometric Dates and their Correlation with Metamorphic events in the Granulite-Facies Basement of the Serre, Southern Calabria (Italy). Contrib. Mineral. Petrol. 73, 23–38.

Schenk, V., 1984. Petrology of Felsic Granulites, Metapelites, Metabasics, Ultramafics, and Metacarbonates from Southern Calabria (Italy): prograde Metamorphism, uplift and cooling of a former lower Crust. J. Petrol. 25, 255–298.

Schenk, V., 1989. P-T-t path of the lower crust in the Hercynian fold belt of southern Calabria. Geol. Soc. Spec. Publ. 43, 337–342.

Schenk, V., 1990. The exposed crustal cross section of southern Calabria, Italy: structure and evolution of a segment of Hercynian crust. In: Exposed Cross-Sections of the Continental Crust, pp. 21–42.

Seifert, F., Schreyer, W., 1970. Lower temperature stability limit of Mg Cordierite in the range 1-7 kb water pressure: a redetermination. Contrib. Mineral. Petrol. 27, 225–238.

Sibson, R.H., 1975. Generation of Pseudotachylyte by Ancient Seismic Faulting. Geophys. J. R. Astron. Soc. 43 (3), 775–794. https://doi.org/10.1111/j.1365-246X.1975.tb06195.x.

Spiegel, C., 2003. Mylonitization, dry shearing and the exhumation of the former lower crust: the Curinga-Girifalco Line (Calabria, South Italy). Neues Jahrbuch Fur Geologie Und Palaontologie - Abhandlungen. https://doi.org/10.1127/njgpa/230/2003/359.

Spray, J.G., 2010. Frictional melting processes in planetary materials: from hypervelocity impact to Earthquakes. Annu. Rev. Earth Planet. Sci. 38 (1), 221–254. https://doi.org/10.1146/annurev.earth.031208.100045.

Stähle, V., 1975. Natural shock behavior of Almandite in Metamorphic rocks from the Ries Crater, Germany. Earth Planet. Sci. Lett. 25, 71–81.

Ujiie, K., Yamaguchi, H., Sakaguchi, A., Toh, S., 2007. Pseudotachylytes in an ancient accretionary complex and implications for melt lubrication during subduction zone earthquakes. J. Struct. Geol. 29 (4), 599–613. https://doi.org/10.1016/j.jsg.2006.10.012.

Venkatesh, V., 1952. Development and growth of cordierite in Para-lavas. Am. Mineral. 37 (9–10), 831–848.

Verschure, R.H., Andriessen, P.A.M., Boelrijk, N.A.I.M., Hebeda, E.H., Maijer, C., Priem, H.N.A., Verdurmen, E.A.T., 1980. On the thermal stability of Rb-Sr and K-Ar biotite systems: evidence from coexisting Sveconorwegian (ca 870 Ma) and Caledonian (ca 400 Ma) biotites in SW Norway. Contrib. Mineral. Petrol. 74 (3), 245–252. https://doi.org/10.1007/BF00371694.

Zack, T., Hogmalm, K.J., 2016. Laser ablation Rb/Sr dating by online chemical separation of Rb and Sr in an oxygen-filled reaction cell. Chem. Geol. 437, 120–133. https://doi.org/10.1016/j.chemgeo.2016.05.027.

Zhong, X., Petley-Ragan, A.J., Incel, S.H.M., Dabrowski, M., Andersen, N.H., Jamtveit, B., 2021. Lower crustal earthquake associated with highly pressurized frictional melts. Nat. Geosci. https://doi.org/10.1038/s41561-021-00760-x.